Article

Not peer-reviewed version

Upconverting Nanoparticles Functionalized with Protein-Gold Nanoclusters and Chlorin e6 for Near-Infrared Activated Photodynamic Therapy

Vilius Poderys , Greta Butkiene , Dziugas Jurgutis , Aleja Marija Daugelaite , Egle Ezerskyte , Vaidas Klimkevicius , Vitalijus Karabanovas *

Posted Date: 17 March 2026

doi: 10.20944/preprints202603.1240.v1

Keywords: protein corona; cancer; PDT; reactive oxygen species; energy transfer

 doi:10.20944/preprints202603.1240.v1

Article

Upconverting Nanoparticles Functionalized with Protein-Gold Nanoclusters and Chlorin e6 for Near-Infrared Activated Photodynamic Therapy

Vilius Poderys [1], Greta Butkiene [1], Dziugas Jurgutis [1], Aleja Marija Daugelaite [1,2], Egle Ezerskyte [2], Vaidas Klimkevicius [1,2] and Vitalijus Karabanovas [1,3,*]

[1] Biomedical Physics Laboratory, National Cancer Institute, P. Baublio str. 3b, LT-08406, Vilnius, Lithuania;

[2] Institute of Chemistry, Faculty of Chemistry and Geosciences, Vilnius University, Naugarduko str. 24, LT-03225, Vilnius, Lithuania;

[3] Department of Chemistry and Bioengineering, Vilnius Gediminas Technical University, Sauletekio av. 11, LT-10221, Vilnius, Lithuania;

* Correspondence: vitalijus.karabanovas@nvi.lt

Abstract

Current efforts in improving photodynamic therapy focus on nanomaterials that integrate deep-tissue imaging with efficient reactive oxygen species generation. Gold nanoclusters (Au NCs) are promising alternatives to conventional photosensitizers due to their effective ROS production and enhanced biocompatibility when stabilized by protein corona. However, both photosensitizers and Au NCs are typically activated by ultraviolet or visible light, which cannot penetrate deeper into tissues and is limited to superficial applications. Here, we report a near-infrared (NIR)-activated photodynamic nanoplatform based on core-shell upconverting nanoparticles (UCNPs; $NaGdF_4$:Yb^{3+},Er^{3+}@$NaGdF_4$:Yb^{3+},Nd^{3+}), functionalized with a protein corona containing bovine serum albumin-stabilized Au NCs (BSA-Au NCs) and photosensitizer chlorin e6 (Ce6). Spectroscopic data confirmed the formation of the UCNP-BSA-Au-Ce6 nanoplatform and demonstrated 32% energy transfer efficiency from UCNPs to Ce6, resulting in efficient reactive oxygen species generation under 808 nm irradiation. Cellular experiments confirmed effective internalization and optimal biocompatibility of the nanoplatform in human breast cancer and healthy cells. Upon 808 nm irradiation, the nanoplatform significantly reduced viability of MDA-MB-231 cancer cells. These findings indicate that the UCNP-BSA-Au-Ce6 nanoplatform couples NIR activation with enhanced singlet oxygen production, providing a multifunctional platform for deep-tissue imaging and NIR-activated photodynamic therapy.

Keywords: protein corona; cancer; PDT; reactive oxygen species; energy transfer

1. Introduction

Photodynamic therapy (PDT) is an established cancer treatment method that employs light-activated compounds, known as photosensitizers (PS), which produce reactive oxygen species (ROS) upon exposure to light [1]. The generated ROS cause cellular damage that could lead to the death of cancer cells during PDT. However, most PS have several disadvantages, such as nonspecific accumulation in healthy tissues, low water solubility, low photostability, and cytotoxicity. Although newer PS have been developed to mitigate many of these limitations, achieving selective accumulation of PS in tumor tissues remains a major challenge [2].

Rapid development of nanotechnology in the past decades has also offered innovative solutions for cancer diagnostic and treatment. There have been many efforts devoted to research on creating nanomaterials, which could produce ROS upon irradiation with light and be applied for PDT. Among the wide spectrum of nanomaterials investigated, gold nanoclusters (Au NCs) have attracted

 doi:10.20944/preprints202603.1240.v1

significant attention in the scientific community as promising agents for cancer therapy. Currently, Au NCs are among the few nanomaterials capable of competing with PS in terms of ROS generation [3,4]. Protein-stabilized Au NCs are particularly attractive due to their environmentally friendly synthesis and biocompatibility [5]. A variety of proteins can be used for Au NCs synthesis [6,7], including bovine serum albumin (BSA) [6] and human serum albumin (HSA) [8,9]. BSA and HSA are homologous proteins with similar functions, such as transport of small molecules and the maintenance of osmotic balance, but they differ in specific properties, including hydrophobicity, stability, and crystallization behaviour [10]. The lower cost and availability of BSA have led to extensive research on BSA-stabilized gold nanoclusters (BSA–Au NCs), resulting in a better understanding of these systems compared with other protein-stabilized Au NCs. Previously our group demonstrated the biocompatibility of BSA-Au NCs and their accumulation in cancer cells [11], as well as ROS generation and destruction of cancer cells upon visible (VIS) light irradiation *in vitro* [4]. In addition, we showed that BSA-Au NCs are eliminated through the urinary system *in vivo* [12]. Furthermore, we demonstrated that Au NCs can be synthesized in human blood plasma, and the obtained Au NCs exhibit properties similar to those of BSA-Au NCs. This suggests that personalized Au NCs could potentially be applied to patients in the future [13].

BSA-Au NCs could be a promising agent for PDT, however, their activation with ultraviolet (UV) or visible light limits their application to superficial tissues. In contrast, near-infrared (NIR) light can penetrate deeper into biological tissues but lacks sufficient energy for direct excitation of BSA-Au NCs via single-photon absorption. BSA-Au NCs can be excited by NIR light via a two-photon absorption process [14]; however, this approach requires expensive ultrafast lasers and high-speed scanning systems. Additionally, it is often difficult to avoid thermal effects due to the extremely high laser power densities required for non-linear excitation. To address these limitations, upconverting nanoparticles (UCNPs) offer a promising solution [15]. The upconverted emission from excited UCNPs can be transferred to BSA-Au NCs, promoting their excitation and subsequent generation of ROS required for PDT. This mechanism enables deeper tissue penetration while maintaining the ability to activate BSA-Au NCs. A key advantage of such a nanoplatform is that UCNPs excitation could be achieved via steady-state NIR lasers at relatively low power densities compared to those required for two-photon excitation.

Once nanoparticles are exposed to protein-rich media, the formation of a protein corona (sometimes referred as biomolecular corona [16]) around the nanoparticle surface begins. The protein corona can alter nanoparticle properties and determine their interaction with the biological environment [17]. Surface modification of nanoparticles and composition of the surrounding media are the main factors determining protein corona [18,19]. Despite extensive research, current knowledge of the protein corona remains insufficient to accurately predict the behaviour of nanoparticles after their administration to an organism [20]. Two main strategies are commonly used to minimize undesirable effects associated with protein corona formation: preventing protein adsorption or controlling it. The first strategy involves the modification of the nanoparticle surface to reduce protein binding. Various approaches have been proposed, although the polyethylene glycol functionalization is the most widely used [21]. However, complete elimination of protein adsorption on nanoparticle surfaces remains challenging [20]. Alternatively, a protein corona can be intentionally formed under controlled conditions using selected proteins prior to *in vitro* or *in vivo* applications. For example, controlled formation of BSA protein corona on UCNPs improves their colloidal and physiological stability and can serve as a delivery platform for loading various therapeutic agents [22,23]. To the best of our knowledge, no nanoplatforms based on UCNPs combined with BSA–Au NCs have been reported to date.

In this study, BSA-Au NCs were used to form a protein corona around core-shell UCNPs ($NaGdF_4:Yb^{3+},Er^{3+}@NaGdF_4:Yb^{3+},Nd^{3+}$). This system was designed to combine the deep tissue penetration of NIR light with the ROS-generating capability of the nanoclusters. The ability of the UCNP-BSA-Au nanoplatform to generate ROS was evaluated using fluorescent ROS sensor dihydrorhodamine 123 (DHR123). However, ROS generation by the UCNP–BSA–Au nanoplatform

 doi:10.20944/preprints202603.1240.v1

under NIR irradiation was insufficient to achieve effective photodynamic activity. To enhance ROS generation, a complex of BSA-Au NCs and photosensitizer chlorin e6 (Ce6) was prepared prior to its assembly as a protein corona on UCNPs. Upon NIR irradiation, the UCNP-BSA-Au-Ce6 nanoplatform exhibited significantly higher ROS generation and improved performance compared to the nanoplatform without Ce6. Additionally, the cellular accumulation of nanoplatforms was evaluated in breast cancer and healthy cells. The results showed that the nanoplatforms were internalized into cells and did not exhibit cytotoxicity in the absence of NIR irradiation. In contrast, treatment with UCNP-BSA-Au-Ce6 nanoplatform followed by irradiation with an 808 nm laser significantly reduced cancer cells' viability, indicating its potential as a phototherapeutic agent for NIR-activated photodynamic therapy.

2. Materials and Methods

In this study, $NaGdF_4:Yb^{3+}(18\%),Er^{3+}(2\%)@NaGdF_4:Yb^{3+}(5\%),Nd^{3+}(40\%)$ core-shell UCNPs were used. These core-shell UCNPs were synthesized via a two-step thermal coprecipitation route following a procedure previously reported by our research group [24]. BSA-Au NCs were synthesized according to the protocol described by Xie et al. [6], with minor modifications. Oleate ligands were removed from UCNPs surfaces by treatment under acidic conditions, resulting in the water-dispersible nanoparticles. The ligand-free UCNPs were then immersed in a solution containing BSA-Au NCs or BSA-Au NCs with the photosensitizer Ce6 to form a protein corona. The generation of ROS and singlet oxygen by the UCNP–BSA–Au and UCNP–BSA–Au–Ce6 nanoplatforms under 808 nm laser irradiation was evaluated using the fluorescent probes DHR123 (ROS) and SOSG (singlet oxygen). Detailed methodologies describing the synthesis and characterization of UCNPs and BSA-Au NCs, as well as the procedures for the preparation of UCNP-BSA-Au and UCNP-BSA-Au-Ce6 nanoplatforms and the assessments of their physicochemical properties, are provided in the Supplementary Materials.

Cellular experiments included conditions for the cultivation of breast cancer and healthy breast epithelial cells. The cellular accumulation of UCNPs in these cells was visualized by confocal laser scanning microscopy. PDT effect was evaluated *in vitro* using MDA-MB-231 cancer cells. Cell viability after incubation with nanoparticles and irradiation with 808 nm laser was assessed using fluorescent viability dyes: Calcein-AM (Invitrogen) for live-cell staining and propidium iodide (PI; Carl ROTH, Karlsruhe, Germany) for dead-cell staining. Additionally, cell metabolic activity was measured using the Cell Counting Kit-8 (CCK-8; Vazyme, China). Detailed descriptions of all cellular experimental procedures are provided in Supplementary Materials.

3. Results and Discussion

3.1. Formation of UCNP-BSA-Au Nanoplatform and ROS Generation

Firstly, $NaGdF_4:Yb^{3+},Er^{3+}@NaGdF_4:Yb^{3+},Nd^{3+}$ core-shell UCNPs were freshly synthesized and spectroscopically evaluated. Figure 1A represents upconversion emission spectrum of nanoparticles dispersed in aqueous media (DI water pH=5.5). Upon excitation with continuous wave 808 nm laser, the emission spectra exhibit five major emission bands in UV-VIS region, which are characteristic of Er^{3+} electronic transitions. The observed emission peaks correspond to the following transitions: $^4G_{11/2}\rightarrow{}^4I_{15/2}$ (ca. 377 nm), $^2H_{9/2}\rightarrow{}^4I_{15/2}$ (ca. 407 nm), $^2H_{11/2}\rightarrow{}^4I_{15/2}$ (ca. 519 nm), $^4S_{3/2}\rightarrow{}^4I_{15/2}$ (ca. 539 nm), and $^4F_{9/2}\rightarrow{}^4I_{15/2}$ (ca. 653 nm). The upconversion emission process in $NaGdF_4:Yb^{3+},Er^{3+}@NaGdF_4:Yb^{3+},Nd^{3+}$ core-shell UCNPs is initiated by the absorption of 808 nm photons by Nd^{3+} located in the outer shell layer. The photons from exited states of Nd^{3+} ($^4F_{5/2}$, $^4F_{3/2}$) are transferred to neighboring Yb^{3+} ($^2F_{5/2}$). The excited Yb^{3+} serve as intermediate sensitizers and could effectively transfer energy and populate higher–lying energy states of Er^{3+} located in core of UCNPs. Radiative relaxation from excited levels of Er^{3+} to the ground state ($^4I_{15/2}$) results in the characteristic emission band in UV-blue, green and red range of upconversion emission spectra. A detailed energy-level scheme and the corresponding optical transitions have been reported in our previous publication [24].

 doi:10.20944/preprints202603.1240.v1

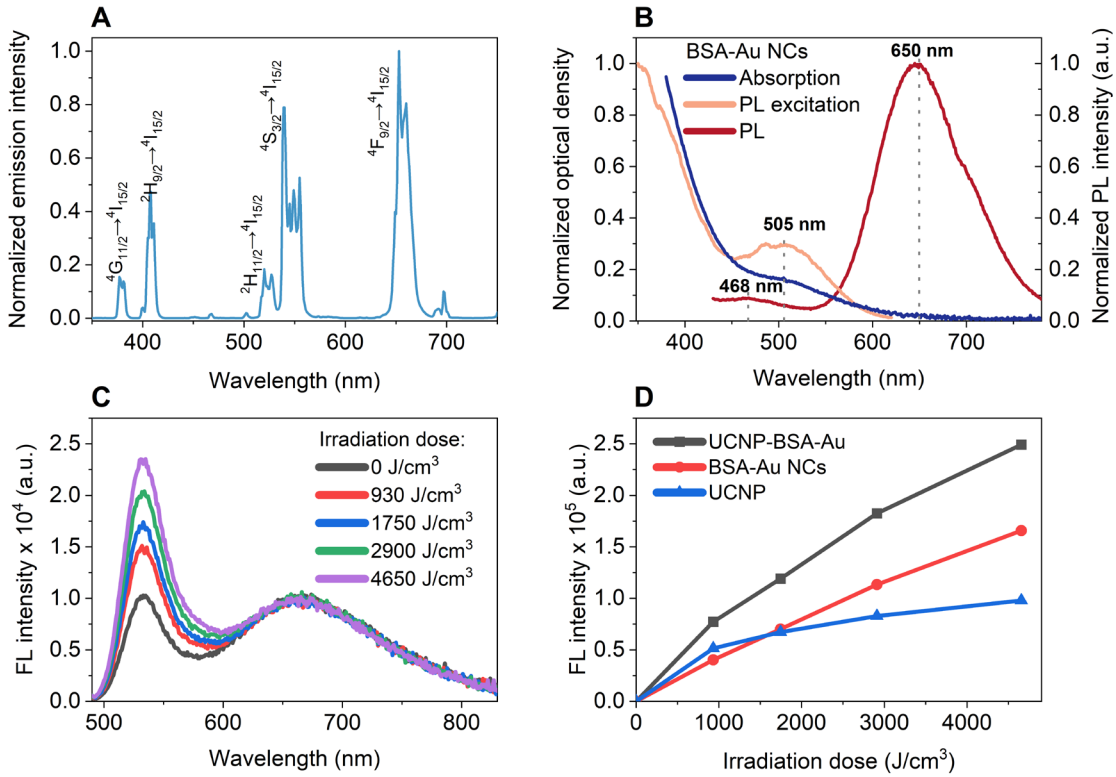

Figure 1. (A) An emission spectrum of $NaGdF_4:Yb^{3+},Er^{3+}$@$NaGdF_4:Yb^{3+},Nd^{3+}$ core–shell UCNPs in the UV/VIS region (λ_{ex}= 808 nm). (B) Spectroscopic analysis of BSA-Au NCs: absorption (blue), PL excitation (light orange, λ_{em}= 650 nm) and PL (red, λ_{ex}= 405 nm). (C) Evolution of Rh123 fluorescence spectrum (λ_{ex}=480 nm) during irradiation of formed UCNP-BSA-Au nanoplatform with 808 nm laser. (D) Changes in integrated Rh123 fluorescence (515-550 nm, λ_{ex}=480 nm) during 808 nm laser irradiation for three samples: UCNP-BSA-Au nanoplatform (black), BSA-Au NCs (red) and UCNPs (blue).

Secondly, BSA-stabilized gold nanoclusters were synthesized and spectroscopically evaluated. The absorption, photoluminescence (PL) excitation, and PL spectra of the BSA-Au NCs are presented in Figure 1B. The synthesized BSA-Au NCs exhibit a pronounced PL band in the red spectral region with a maximum at approximately 650 nm, accompanied by a weaker emission band centered at around 468 nm. The PL excitation spectrum shows a distinct band with a maximum at 505 nm. The absorption spectrum does not display defined absorption peaks; however, a shoulder is observed in the region at around 505 nm, coinciding with the PL excitation maximum. Overall, the absorption increases toward shorter wavelengths, which is characteristic of ultrasmall Au NCs lacking a surface plasmon resonance band.

The presence of a PL maximum at 650 nm confirms successful formation of BSA-Au NCs. The number of gold atoms in the cluster can be estimated using the relation [25]:

$$N = \left(\frac{e\lambda_{\max}E_F}{hc}\right)^3, \quad (1)$$

where N is the number of gold atoms in the nanocluster, $\lambda_{\max}$ is the maximum of the fluorescence emission band, E_F is the Fermi energy of gold expressed in eV, e is the elementary charge, h is Planck's constant, and c is the speed of light.

Using this equation, the synthesized BSA-Au NCs were estimated to contain approximately 24 gold atoms per nanocluster. This value is in good agreement with literature reports, particularly the study by Xie et al. (2009), which describes the formation of $Au_{(25)}$ clusters under similar synthesis conditions [6].

Efficient formation of BSA-Au NCs protein corona around UCNPs, as well as subsequent energy transfer processes, requires close interparticle interactions governed primarily by surface chemistry

 doi:10.20944/preprints202603.1240.v1

or electrostatic forces. Therefore, surface charge characteristics of both components were evaluated by measuring their zeta potential as a function of pH. The zeta potentials of BSA-Au NCs and UCNPs were determined over a pH range of 3–11 (Suppl. Matt. Figure S1). Across the pH range of 5-10, the BSA-Au NCs exhibited a negative zeta potential, indicating an overall negatively charged surface. The isoelectric point (IEP) was identified at pH 4.2, where the net surface charge approaches zero, leading to reduced colloidal stability due to aggregation. At pH values below 4.2, the zeta potential becomes positive. The measured IEP is in close agreement with reported values for native BSA (pI ≈ 4.5) [26], indicating that incorporation of Au NCs within the protein matrix does not significantly perturb the intrinsic electrochemical properties of BSA. This observation suggests preservation of the protein structure and supports the expected biocompatibility of the synthesized BSA-Au NCs.

The pH-dependent zeta potential profile of UCNPs (Suppl. Matt. Figure S1) reveals an isoelectric point at significantly higher pH compared to BSA-Au NCs, identified at pH 8.5. At alkaline pH (pH > 9), UCNPs exhibit a negative surface charge, whereas at lower pH values the surface becomes positively charged.

During preparation of UCNP–BSA-Au nanoplatform, the UCNPs solution was adjusted to pH 5.5, at which the zeta potential was approximately +44 mV, indicating a strongly positively charged surface. In contrast, BSA-Au NCs dispersed at pH 7.4 exhibited a negative zeta potential of approximately −22 mV. Upon mixing, the resulting dispersion acquired an intermediate pH between 5.5 and 7.4. Within this pH range, UCNPs remain positively charged while BSA-Au NCs remain negatively charged, establishing favorable electrostatic conditions for adsorption. The oppositely charged surfaces promote attractive interactions, leading to spontaneous formation of a BSA-Au NCs protein-based corona around the UCNPs.

To experimentally verify this electrostatically driven association, centrifugation-based separation experiments were performed. Dispersions containing UCNPs, BSA-Au NCs, or their mixtures were centrifuged at 14,500 RPM, and PL spectra were recorded for the initial sample (control) as well as for the supernatant and the redispersed pellet after centrifugation. BSA-Au NCs alone did not sediment under the applied centrifugal force, and no pellet was formed, indicating homogeneous distribution of nanoclusters throughout solution. In contrast, UCNPs alone exhibited negligible emission in the supernatant and strong UC emission in the redispersed pellet, confirming efficient sedimentation due to their larger size and higher mass.

For the UCNP–BSA-Au nanoplatform, a pronounced redistribution of BSA-Au NCs PL was observed after centrifugation (Supplementary Materials Figure S2). PL intensity associated with BSA-Au NCs was significantly reduced in the supernatant and correspondingly increased in the redispersed pellet. This behavior observed in UCNP and BSA-Au NCs mixture indicates co-sedimentation of BSA-Au NCs with UCNPs and therefore confirms adsorption of the nanoclusters onto the UCNP surface. Additionally, emission measurements of the centrifuged UCNP–BSA-Au nanoplatform samples revealed negligible signal in the supernatant fraction, further supporting efficient sedimentation of UCNP-containing nanoplatforms. Collectively, these results demonstrate that electrostatic attraction between positively charged UCNPs and negatively charged BSA-Au NCs drives spontaneous surface decoration and the formation of a stable UCNP–BSA-Au nanoplatform. Although the qualitative formation of the nanoplatform is clearly evidenced, the exact surface coverage and quantitative loading of BSA-Au NCs on UCNPs cannot be directly determined from centrifugation experiments alone.

It has been previously reported that BSA–Au NCs generate ROS upon excitation with blue light [4]. Because the PL excitation spectrum of BSA–Au NCs overlaps with the emission bands of UCNPs, it can be anticipated that UCNPs may act as energy donors for the nanoclusters via an energy-transfer process (Suppl. Matt. Figure S3A). Such a mechanism could potentially enable ROS generation under NIR excitation via upconversion-mediated activation of UCNP–BSA–Au. To test this hypothesis, ROS generation in the UCNP–BSA–Au nanoplatform was investigated using the ROS-sensitive probe DHR123, which is oxidized by ROS to the fluorescent dye rhodamine 123. The changes in the fluorescence spectra of the DHR123 probe during irradiation of UCNP–BSA–Au nanoplatform with

 doi:10.20944/preprints202603.1240.v1

an 808 nm laser are presented in Figure 1C. NIR irradiation of the UCNP–BSA–Au nanoplatform leads to a gradual increase in the fluorescence intensity of the Rh123 band centered at ~525 nm (Figure 1D). This increase indicates that ROS are generated in the solution when the complex is excited with 808 nm radiation. However, the magnitude of fluorescence growth is relatively small. Only a minor difference is observed when comparing the signal increase in the UCNP–BSA–Au nanoplatform sample with that of the control samples containing either UCNPs or BSA–Au NCs alone (Figure 1D). These results suggest that although ROS generation can be detected under 808 nm excitation, the efficiency of ROS production in the UCNP–BSA–Au nanoplatform is low. The weak increase of the DHR123 fluorescence signal indicates that the indirect excitation of BSA–Au NCs mediated by UCNPs emission does not lead to efficient ROS generation under the applied experimental conditions.

To evaluate the occurrence of energy transfer from UCNPs to BSA–Au NCs, the PL decay kinetics of UCNP emission were measured for both ligand-free UCNPs and UCNPs surrounded by a BSA–Au NC corona. The decay kinetics were analyzed for the characteristic UCNPs emission bands at 407 nm, 549 nm and 653 nm (Suppl. Matt. Figure S4). The decay curves were fitted using a bi-exponential model, which is commonly applied to describe the population dynamics and relaxation processes of excited states in UCNPs. The first exponential component exhibits a negative amplitude, indicating a rise component that reflects the population build-up dynamics of the emitting level rather than its relaxation. In UCNP systems, this component is typically associated with excited-state population processes governed by the energy transfer upconversion (ETU) mechanism. The second exponential component corresponds to the decay of the populated excited state and therefore reflects the relaxation dynamics of the emitting level, including radiative emission, non-radiative processes, or energy transfer. A shortening of the lifetime of this second decay component (τ_2) is an indication of the presence of an additional relaxation pathway associated with energy transfer from the excited UCNP states. The decay parameter τ_2 determined for UCNPs was 74, 119, and 213 μs, for emission bands at approximately 407, 549 and 653 nm, respectively. For UCNPs surrounded by BSA–Au NCs corona, the corresponding τ_2 decay times was 76 μs (407 nm), 126 μs (549 nm), and 213 μs (653 nm). Non-radiative energy transfer from UCNPs to BSA-Au NCs would be expected to result in shortening of τ_2 decay lifetime. However, the decay time τ_2 measured for ligand-free UCNPs and for the UCNP–BSA–Au nanoplatform are virtually identical within experimental uncertainty. This indicates that the presence of BSA–Au NCs does not introduce an additional non-radiative relaxation pathway for the excited states of UCNP, suggesting that non-radiative energy transfer from UCNPs to BSA–Au NCs is either absent or extremely inefficient. These observations imply that excitation of the BSA-Au NCs in the nanoplatform most likely occurs via radiative processes, namely through the reabsorption of UCNPs emission by the BSA–Au NCs. Such mechanisms are significantly less efficient than non-radiative mechanisms such as Förster resonance energy transfer (FRET). Although partial spectral overlap between UCNPs emission and the absorption of BSA–Au NCs enables indirect excitation of the nanoclusters, this process leads to only weak activation of the clusters and consequently inefficient ROS generation in the UCNP–BSA–Au nanoplatform under NIR (808 nm) excitation.

3.2. UCNP-BSA-Au-Ce6 Nanoplatform Formation, Investigation of Energy Transfer and Singlet Oxygen Generation

Since the UCNPs with BSA–Au NCs corona did not exhibit efficient ROS generation under NIR excitation, an additional strategy was explored to enhance the photodynamic activity of the system. For this purpose, Ce6, a clinically approved PS capable of generating singlet oxygen, was introduced into the UCNP–BSA–Au NC nanoplatform. Ce6 has been widely used in PDT and is known to interact with BSA, which can facilitate its binding to nanoparticle with protein corona [27].

Fluorescence spectra (λ_{ex} =405 nm) of free Ce6 in water and in an aqueous solution containing BSA–Au NCs are presented in Figure 2A. The spectra reveal a clear change in the emission characteristics of Ce6 in the presence of the BSA-Au NCs. The fluorescence maximum of free Ce6 in aqueous solution is observed at approximately 661 nm. However, after the addition of Ce6 to the

 doi:10.20944/preprints202603.1240.v1

UCNP–BSA–Au nanoplatform, a red shift of the fluorescence band was detected, with the Ce6 fluorescence band maximum shifting to 667 nm at a BSA-Au NCs:Ce6 ratio of 1:1. Such a bathochromic shift is consistent with literature reports describing the interaction of Ce6 with BSA molecules [27] and indicates binding of Ce6 to the protein component of the corona. As the Ce6 concentration was gradually increased, the fluorescence maximum shifted back toward shorter wavelengths (data not presented), approaching the position characteristic of free Ce6. This behavior indicates saturation of the available binding sites within the protein corona.

Interaction between Ce6 and the protein corona, should create favorable conditions for energy transfer from UCNPs to Ce6. The emission band of UCNPs at 407 and 653 nm significantly overlaps with the absorption spectrum of Ce6 (Suppl. Matt. Figure S3B), suggesting that energy transfer from the UCNP blue and red emission band to Ce6 is feasible. To evaluate this possibility, PL decay kinetics of the UCNPs emission bands were measured while gradually increasing the Ce6 concentration (Suppl. Matt. Figure S4). The decay kinetics of the blue (407 nm) and green (549 nm) UCNP emission bands showed almost no change with increasing the Ce6 concentration, although a slight shortening of the lifetime was observed for the 407 nm band, suggesting a minor contribution of energy transfer from this UCNP energy state to Ce6 (Suppl. Matt. Figure S4 A and B). In contrast, a pronounced shortening of the lifetime of the red UCNP emission band at 653 nm was observed as the Ce6 concentration increased (Figure 2B). The τ_2 lifetime of this emission band decreased progressively from 213.2 μs to 145 μs until a molar UCNP:Ce6 ratio of approximately 1:10 was reached (Suppl. Matt. Table S1). Further increases in Ce6 concentration did not produce additional changes in the decay time. This saturation behavior indicates that only a limited number of Ce6 molecules are located within the effective energy-transfer distance from the UCNP surface. The observed plateau at the UCNP:Ce6 molar ratio of approximately 1:10 suggests that up to ten Ce6 molecules can be positioned in close proximity to each nanoparticle. Considering that Ce6 interacts with BSA with an approximately 1:1 binding stechiometry [27], this result allows estimation of the number of BSA–Au NCs forming the protein corona around each UCNP. The obtained value indicates that the corona surrounding a single UCNP is composed of approximately ten BSA–Au NCs, which is consistent with the expected packing density based on their reported hydrodynamic size.

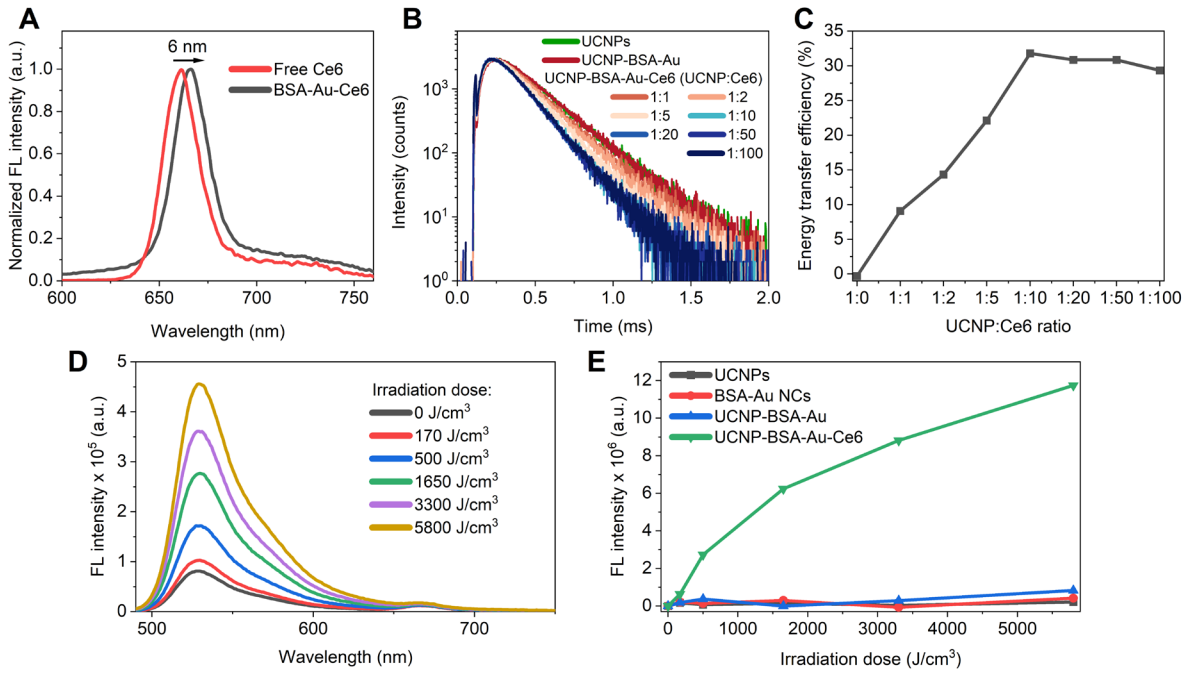

Figure 2. (A) Fluorescence spectra of free Ce6 and Ce6 bound to UCNP-BSA-Au nanoplatform. The shift of fluorescence band confirms Ce6 interaction with BSA (λ_{ex}=405 nm). (B) UCNPs emission decay kinetics of 653 nm emission band in different samples: UCNPs, UCNP-BSA-Au nanoplatform and UCNP-BSA-Au-Ce6 with

 doi:10.20944/preprints202603.1240.v1

various UCNP:Ce6 ratios. (C) Energy transfer efficiency from UCNP band at 653 nm to Ce6 as a function of the UCNP:Ce6 ratio. (D) Evolution of SOSG-EP fluorescence spectrum (λ_{ex}=480 nm) during irradiation of UCNP-BSA-Au-Ce6 nanoplatform with 808 nm laser. (E) Changes in integrated SOSG-EP fluorescence (515-550 nm, λ_{ex}=480 nm) during 808 nm laser irradiation for four samples: UCNPs (black), BSA-Au NCs (red), UCNP-BSA-Au nanoplatform (blue), and UCNP-BSA-Au-Ce6 (green).

The efficiency of energy transfer from the donor to the acceptor can be calculated from the change in the excited-state relaxation lifetime [28]:

$$\eta = \left(1 - \frac{\tau_{UCNP-BSA-Au-Ce6}}{\tau_{UCNP}}\right), \quad (2)$$

where η is the energy transfer efficiency, $\tau_{UCNP\text{-}BSA\text{-}Au\text{-}Ce6}$ is the τ_2 PL emission decay time of UCNPs-BSA-Au-Ce6 nanoplatform, and τ_{UCNP} is the τ_2 PL emission decay time of ligand-free UCNPs.

The energy transfer efficiencies for various UCNPs:Ce6 ratios (presented in Table 1).

Table 1. Efficiency of energy transfer from UCNP emission bands at 407 nm and 653 nm to Ce6.

UCNP Emission Band	UCNP:Ce6 ratio						
	1:1	1:2	1:5	1:10	1:20	1:50	1:100
407 nm	0%	0%	3%	7%	9%	8%	9%
653 nm	9%	14%	22%	32%	31%	31%	29%

Energy transfer efficiency from blue UCNPs emission band at 407 nm was negligible, whereas energy transfer from the red UCNPs emission band at 653 nm increased with UCNP:Ce6 ratio and reached maximum of approximately 32% at a ratio of 1:10. These results shows that non-radiative energy transfer occurs from the red UCNPs emission band to Ce6 molecules bound within the BSA-Au NCs corona formed on UCNPs. Since Ce6 is an efficient singlet oxygen generator, this energy-transfer pathway suggests that this complex, in which Ce6 is incorporated into the UCNP–BSA–Au nanoplatform corona, can function as an effective photosensitising system. Consequently, NIR excitation of UCNPs can activate Ce6 via upconvertion-mediated energy transfer, enabling singlet oxygen generation and potentially enhancing the photodynamic therapeutic performance of the system. Production of singlet oxygen in prepared UCNP–BSA–Au–Ce6 nanoplatform was evaluated using the Singlet Oxygen Sensor Green (SOSG) probe. SOSG reacts with singlet oxygen to form a fluorescent endoperoxide product (SOSG-EP). The formation of SOSG-EP was monitored by measuring the fluorescence intensity of its emission band (λ_{max} = 529 nm). Changes in SOSG-EP fluorescence during irradiation of the samples with an 808 nm laser are shown in Figure 2D–E.

Only a minor increase in the SOSG-EP fluorescence was observed upon irradiation of UCNPs, BSA–Au NCs, and UCNP-BSA-Au nanoplatform, indicating that these systems do not produce detectable amounts of singlet oxygen under the applied conditions. In contrast, a pronounced increase in the SOSG-EP fluorescence intensity was detected in the UCNP–BSA–Au–Ce6 nanoplatform under identical irradiation conditions.

The significant increase in SOSG fluorescence demonstrates efficient singlet oxygen generation only when Ce6 molecules are incorporated into the protein corona surrounding the UCNPs. The observed effect is consistent with the previously identified energy transfer pathway from the red UCNP emission band to Ce6, which activates the photosensitizer and triggers singlet oxygen production.

These results indicate that the UCNP–BSA–Au–Ce6 nanoplatform represents a promising system for NIR-activated PDT. The possibility of excitation with NIR radiation enables PDT at greater tissue depths and expands the potential of such nanostructured theranostic platforms combining PL imaging and PDT.

 doi:10.20944/preprints202603.1240.v1

3.3. Accumulation in Cells

Before any biological application of nanoparticles, it is essential to investigate whether they can internalize into cells. For biological testing, we used the breast cancer cell lines MDA-MB-231 and MCF-7, as well as the MCF-10A cell line which represents healthy breast epithelial cells. Confocal microscopy analysis revealed that UCNPs, UCNP-BSA-Au and UCNP-BSA-Au-Ce6 nanoplatforms accumulated in MDA-MB-231, MCF-7, and MCF-10A cells (Figure 3). The UCNP emission was detected in cluster- or vesicle-like structures, indicating an endocytic uptake of the nanoparticles [18]. Visually, there was no difference in accumulation between ligand-free UCNPs and the protein coated nanoplatforms (UCNP-BSA-Au and UCNP-BSA-Au-Ce6). Exposure of nanoparticles to protein-rich media leads to the formation of a protein corona, which alters cellular internalization pathways [18]. In this case, both UCNP–BSA–Au and UCNP–BSA–Au–Ce6 nanoplatforms had already formed a hard protein corona prior to introduction into the cell culture medium; therefore, only a soft corona could form subsequently. It is also likely that the ligand-free UCNPs were covered by a protein corona primarily composed of BSA, the most abundant protein in fetal bovine serum [18].

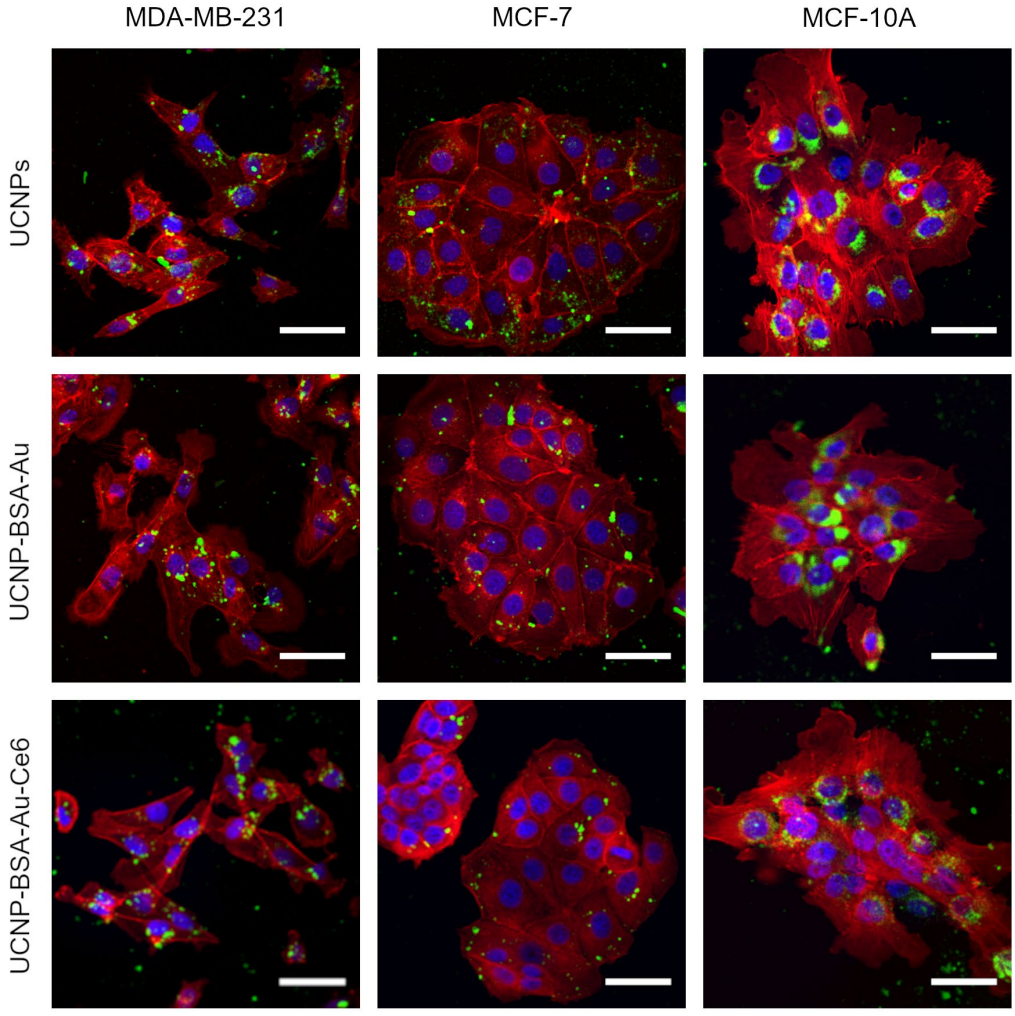

Figure 3. Confocal microscopy images of MDA-MB-231, MCF-7, and MCF-10A cells after incubation with UCNPs, UCNP-BSA-Au, and UCNP-BSA-Au-Ce6 nanoplatforms. UCNP emission is shown in green (λ_{ex}= 808 nm), F-actin stained with CF594 dye is shown in red (λ_{ex}=543 nm), and nuclei stained with Hoechst are shown in blue (λ_{ex}=404 nm). Scale bars**:** 50 μm.

Additionally, UCNPs were coated with BSA conjugated to Alexa555 dye (BSA-Alexa555), to evaluate if BSA coating remains attached to the UCNPs after internalization in cells. The UCNP-BSA-Alexa555 nanoplatform was prepared using the same method as for the UCNP-BSA-Au

 doi:10.20944/preprints202603.1240.v1

nanoplatform, under identical incubation conditions. During confocal microscopy imaging UCNPs emission and Alexa555 fluorescence overlapped within the same intracellular regions (Suppl. Matt. Figure S5). The overlapping signals indicate that UCNP-BSA-Alexa555 nanoplatform remains stable after internalization. Therefore, UCNP-BSA-Au and UCNP-BSA-Au-Ce6 nanoplatforms are also expected to remain conjugated within cells.

The cells after incubation with UCNPs, UCNP-BSA-Au and UCNP-BSA-Au-Ce6 retained unchanged morphology, which indicates that the investigated nanoparticles are biocompatible. These findings were further confirmed by lactate dehydrogenase release assay (Suppl. Matt. Figure S6).

3.4. Photodynamic Effect in Cells

Having determined nanoplatforms accumulation across cell lines, we selected MDA-MB-231 cell line to evaluate the *in vitro* photodynamic efficacy of the UCNP-BSA-Au and UCNP-BSA-Au-Ce6 nanoplatforms. Cells were incubated with 0.1 mg/mL UCNP-BSA-Au or UCNP-BSA-Au-Ce6 nanoplatforms for 24 h and then irradiated with an 808 nm laser. For irradiation, we constructed a custom automated setup based on a modified 3D printer equipped with a microplate holder and an 808 nm diode laser. The system scanned the laser beam across the surface of each well in a line-scanning pattern with 0.5 mm spacing between parallel lines, ensuring uniform and reproducible irradiation of the entire well area. Importantly, laser irradiation alone had no detectable effect on cell viability. Irradiated control cells retained normal morphology (Figure 4A, D), exhibited a high fraction of Calcein-AM positive cells (Figure 4D, G), and showed no significant change in metabolic activity (Figure 4H). These findings confirm that the applied NIR irradiation was harmless. The use of 808 nm excitation is advantageous for PDT, as NIR light penetrates deeper into biological tissues compared with the UV or VIS light required for direct excitation of BSA-Au NC or Ce6 [29]. In addition, irradiation at 808 nm typically produces much lower photothermal effects than the commonly used 980 nm excitation for UCNPs, because water absorbs strongly at 980 nm [30]. Consequently, 808 nm irradiation reduces the risk of local heating and improves the safety profile of NIR-activated PDT, particularly in tissues with high water content [31].

 doi:10.20944/preprints202603.1240.v1

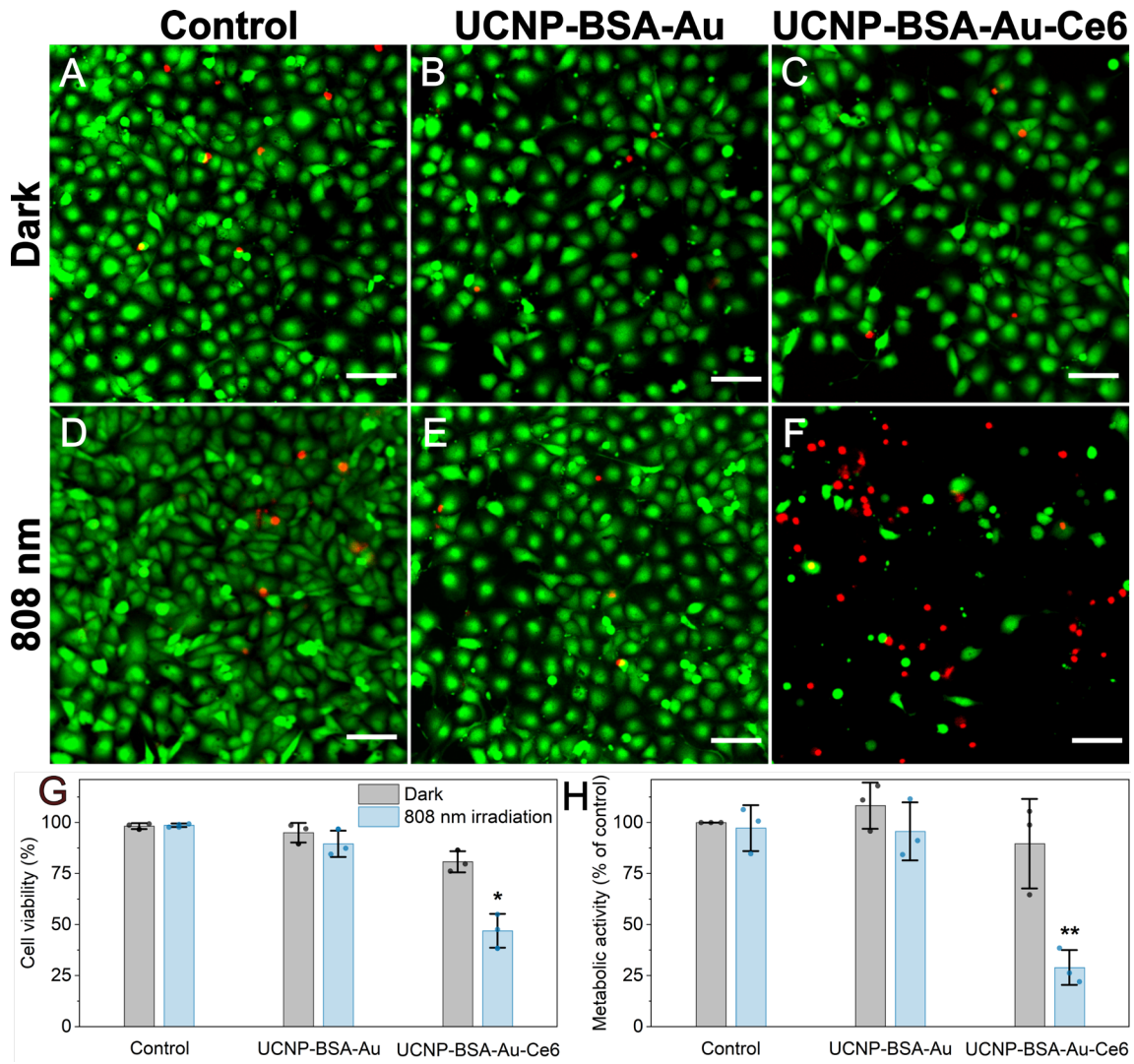

Figure 4. Evaluation of nanoplatform biocompatibility and photodynamic effect in MDA-MB-231 cells. (A–F) Confocal fluorescence images of MDA-MB-231 cells stained with Calcein-AM (live cells, λ_{ex} = 488 nm) and propidium iodide (dead cell nuclei, λ_{ex} = 543 nm) after treatment with UCNP-BSA-Au or UCNP-BSA-Au-Ce6 nanoplatforms and irradiation with an 808 nm laser. Scale bars: 100 μm. (G–H) Quantitative analysis of cell viability and metabolic activity based on the percentage of live cells among total stained cells, determined from Calcein-AM and propidium iodide images using the ImageJ AutoCount macro, and by the CCK-8 assay, respectively. Data points represent the mean of at least three technical replicates per experiment (n = 3 independent experiments). Bars indicate group means ± standard deviation. Statistical significance between the irradiated control and each treatment group was evaluated using a two-sided Welch's *t*-test with Bonferroni correction for multiple comparisons. The non-irradiated control was excluded from statistical comparisons in the CCK-8 assay. Asterisks indicate significant differences from the irradiated control: *$p < 0.05$, **$p < 0.01$.

Cells treated with UCNP-BSA-Au nanoplatform followed by irradiation showed only a slight reduction in viability (89.6 ± 6.4 %) and metabolic activity (95.7 ± 14.2 %) (Figure 4E, G–H) compared to control cells, indicating minimal cytotoxicity of the nanoplatform. In contrast, cells incubated with UCNP-BSA-Au-Ce6 nanoplatform and exposed to 808 nm irradiation exhibited a pronounced photodynamic effect. The number of viable cells decreased, while propidium iodide-positive cells increased compared to non-irradiated controls (Figure 4C, F). Quantitative image analysis and CCK-8 assay confirmed this effect, showing a significant drop in cell viability (47.0 ± 8.3 %) and metabolic activity (29 ± 8.6 %).

In general, *in vitro* PDT typically induces apoptosis as the predominant mechanism of cell death [32]. In our experiments, treatment with the UCNP-BSA-Au-Ce6 nanoplatform followed by

 doi:10.20944/preprints202603.1240.v1

irradiation resulted in clear morphological alterations and a higher number of propidium iodide-positive cells (Figure 4A-F). These observations indicate disruption of plasma membrane integrity, suggesting that photodynamic treatment led to late apoptotic events or secondary necrosis [33].

Collectively, these results demonstrate that the UCNP-BSA-Au-Ce6 nanoplatform effectively mediates NIR-activated PDT. The absence of toxicity in control groups, combined with the strong loss of viability observed only after irradiation of Ce6-containing nanoplatform, supports the proposed energy-transfer mechanism from UCNPs to Ce6, resulting in singlet oxygen generation and subsequent tumor cell death.

4. Conclusions

Combining multiple nanomaterials into a single multifunctional platform can expand their application potential and provide additional advantages. In this study, we described UCNP–BSA–Au–Ce6 nanoplatform that integrates the key features of all three components. UCNPs enable deep-tissue imaging and excitation under NIR irradiation; BSA–Au NCs provide colloidal stability, enhanced biocompatibility, and moderate ROS generation; while Ce6 ensures efficient singlet oxygen production. Specifically, we optimized the formation of the UCNP–BSA–Au–Ce6 nanoplatform and ensured its reproducibility. The high energy transfer efficiency between UCNPs and Ce6 enables effective ROS generation under NIR irradiation, which was successfully confirmed by *in vitro* experiments in breast cancer cells. In contrast, in the absence of irradiation, the UCNP–BSA–Au–Ce6 nanoplatform does not affect cell viability, thereby providing the opportunity to precisely control the treatment area through light activation. Overall, we presented a NIR-activated, ROS-generating multifunctional nanoplatform that may contribute to the further advancement of cancer therapy research.

Supplementary Materials: The following supporting information can be downloaded at the website of this paper posted on Preprints.org, Figure S1: Zeta potential of BSA–Au NCs and ligand-free $NaGdF_4$:Yb,Er@$NaGdF_4$:Yb,Nd UCNPs in water as a function of pH.; Figure S2: Photoluminescence and upconversion emission spectra of the UCNP–BSA–Au nanoplatform before and after centrifugation; Figure S3: Spectral overlap between the UCNP emission (energy donor) and the excitation spectrum of BSA–Au NCs as well as the absorption spectrum of chlorin e6; Figure S4. Photoluminescence decay kinetics of UCNPs, UCNP-BSA-Au and UCNP–BSA–Au–Ce6 nanoplatforms; Table S1: Parameters of UCNPs, UCNP-BSA-Au and UCNP–BSA–Au–Ce6 nanoplatforms emission decays kinetics; Figure S5: Confocal microscopy images of UCNP-BSA-Alexa555 accumulation in MCF-7 cells; Figure S6: Viability of MDA-MB-231, MCF-7 and MCF-10A cells after 24 h and 48 h incubation with 0.1 mg/mL UCNPs, UCNP-BSA-Au and UCNP-BSA-Au-Ce6 nanoplatforms, without exposure to light.

Author Contributions: Conceptualization, V. Karabanovas; validation, V.P., G.B., D.J. and V. Klimkevicius; investigation, V.P., G.B., D.J. A.M.D. and E.E.; resources, V. Klimkevicius and V. Karabanovas; writing—original draft preparation, V.P., G.B. and D.J.; writing—review and editing, A.M.D., E.E., V. Klimkevicius and V. Karabanovas; visualization, V.P., G.B. and D.J.; supervision, V. Karabanovas; project administration, V. Karabanovas; funding acquisition, V. Karabanovas. All authors have read and agreed to the published version of the manuscript.

Funding: This study was financially supported by the Research Council of Lithuania, Grant No. S-MIP-23-5.

Data Availability Statement: The data presented in this study are available on request from the corresponding author.

Conflicts of Interest: The authors declare no conflicts of interest.

Abbreviations

The following abbreviations are used in this manuscript:

Au NCs	Gold nanoclusters

 doi:10.20944/preprints202603.1240.v1

BSA	Bovine serum albumin
CCK-8	Cell counting kit-8
Ce6	Chlorin e6
DHR 123	Dihydrorhodamine 123
EP	Endoperoxide product
FRET	Förster resonance energy transfer
HSA	Human serum albumin
IEP	Isoelectric point
NIR	Near-infrared
PDT	Photodynamic therapy
PEG	Polyethylene glycol
PI	Propidium iodide
PL	Photoluminescence
PS	Photosensitizer
Rh123	Rhodamine 123
ROS	Reactive oxygen species
SOSG	Singlet oxygen sensor green
SOSG-EP	Singlet Oxygen Sensor Green Endoperoxide
UCNP	Upconverting nanoparticle
UV	Ultraviolet
VIS	Visible

References

1. Dougherty, T.J.; Gomer, C.J.; Henderson, B.W.; Jori, G.; Kessel, D.; Korbelik, M.; Moan, J.; Peng, Q. Photodynamic Therapy. *J Natl Cancer Inst* **1998**, *90*, 889–905, doi:10.1093/jnci/90.12.889.
2. Sarbadhikary, P.; George, B.P.; Abrahamse, H. Recent Advances in Photosensitizers as Multifunctional Theranostic Agents for Imaging-Guided Photodynamic Therapy of Cancer. *Theranostics* **2021**, *11*, 9054–9088, doi:10.7150/thno.62479.
3. Cifuentes-Rius, A.; Deepagan, V.G.; Xie, J.; Voelcker, N.H. Bright Future of Gold Nanoclusters in Theranostics. *ACS Appl. Mater. Interfaces* **2021**, *13*, 49581–49588, doi:10.1021/acsami.1c14275.
4. Poderys, V.; Jarockyte, G.; Bagdonas, S.; Karabanovas, V.; Rotomskis, R. Protein-Stabilized Gold Nanoclusters for PDT: ROS and Singlet Oxygen Generation. *Journal of Photochemistry and Photobiology B: Biology* **2020**, *204*, 111802, doi:10.1016/j.jphotobiol.2020.111802.
5. Ahmed, S.; Annu; Ikram, S.; Yudha S., S. Biosynthesis of Gold Nanoparticles: A Green Approach. *Journal of Photochemistry and Photobiology B: Biology* **2016**, *161*, 141–153, doi:10.1016/j.jphotobiol.2016.04.034.
6. Xie, J.; Zheng, Y.; Ying, J.Y. Protein-Directed Synthesis of Highly Fluorescent Gold Nanoclusters. *J Am Chem Soc* **2009**, *131*, 888–889, doi:10.1021/ja806804u.
7. Dixon, J.M.; Egusa, S. Common Motif at the Red Luminophore in Bovine Serum Albumin–, Ovalbumin–, Trypsin–, and Insulin–Gold Complexes. *J. Phys. Chem. Lett.* **2021**, *12*, 2865–2870, doi:10.1021/acs.jpclett.1c00222.
8. Peralta, D.V.; He, J.; Wheeler, D.A.; Zhang, J.Z.; Tarr, M.A. Encapsulating Gold Nanomaterials into Size-Controlled Human Serum Albumin Nanoparticles for Cancer Therapy Platforms. *J Microencapsul* **2014**, *31*, 824–831, doi:10.3109/02652048.2014.940012.
9. Russell, B.A.; Jachimska, B.; Kralka, I.; Mulheran, P.A.; Chen, Y. Human Serum Albumin Encapsulated Gold Nanoclusters: Effects of Cluster Synthesis on Natural Protein Characteristics. *J. Mater. Chem. B* **2016**, *4*, 6876–6882, doi:10.1039/C6TB01827K.
10. Maier, R.; Fries, M.R.; Buchholz, C.; Zhang, F.; Schreiber, F. Human versus Bovine Serum Albumin: A Subtle Difference in Hydrophobicity Leads to Large Differences in Bulk and Interface Behavior. *Crystal Growth & Design* **2021**, *21*, 5451–5459, doi:10.1021/acs.cgd.1c00730.
11. Matulionyte, M.; Dapkute, D.; Budenaite, L.; Jarockyte, G.; Rotomskis, R. Photoluminescent Gold Nanoclusters in Cancer Cells: Cellular Uptake, Toxicity, and Generation of Reactive Oxygen Species. *Int J Mol Sci* **2017**, *18*, E378, doi:10.3390/ijms18020378.

 doi:10.20944/preprints202603.1240.v1

12. Jarockyte, G.; Stasys, M.; Poderys, V.; Buivydaite, K.; Pleckaitis, M.; Bulotiene, D.; Matulionyte, M.; Karabanovas, V.; Rotomskis, R. Biodistribution of Multimodal Gold Nanoclusters Designed for Photoluminescence-SPECT/CT Imaging and Diagnostic. *Nanomaterials* **2022**, *12*, 3259, doi:10.3390/nano12193259.
13. Jarockyte, G.; Poderys, V.; Barzda, V.; Karabanovas, V.; Rotomskis, R. Blood Plasma Stabilized Gold Nanoclusters for Personalized Tumor Theranostics. *Cancers (Basel)* **2022**, *14*, 1887, doi:10.3390/cancers14081887.
14. Raut, S.L.; Shumilov, D.; Chib, R.; Rich, R.; Gryczynski, Z.; Gryczynski, I. Two Photon Induced Luminescence of BSA Protected Gold Clusters. *Chem Phys Lett* **2013**, *561–562*, 74–76, doi:10.1016/j.cplett.2013.01.028.
15. Chen, G.; Qiu, H.; Prasad, P.N.; Chen, X. Upconversion Nanoparticles: Design, Nanochemistry, and Applications in Theranostics. *Chem. Rev.* **2014**, *114*, 5161–5214, doi:10.1021/cr400425h.
16. Monopoli, M.P.; Aberg, C.; Salvati, A.; Dawson, K.A. Biomolecular Coronas Provide the Biological Identity of Nanosized Materials. *Nat Nanotechnol* **2012**, *7*, 779–786, doi:10.1038/nnano.2012.207.
17. Martínez-Negro, M.; González-Rubio, G.; Aicart, E.; Landfester, K.; Guerrero-Martínez, A.; Junquera, E. Insights into Colloidal Nanoparticle-Protein Corona Interactions for Nanomedicine Applications. *Adv Colloid Interface Sci* **2021**, *289*, 102366, doi:10.1016/j.cis.2021.102366.
18. Voronovic, E.; Skripka, A.; Jarockyte, G.; Ger, M.; Kuciauskas, D.; Kaupinis, A.; Valius, M.; Rotomskis, R.; Vetrone, F.; Karabanovas, V. Uptake of Upconverting Nanoparticles by Breast Cancer Cells: Surface Coating versus the Protein Corona. *ACS Appl Mater Interfaces* **2021**, *13*, 39076–39087, doi:10.1021/acsami.1c10618.
19. Richtering, W.; Alberg, I.; Zentel, R. Nanoparticles in the Biological Context: Surface Morphology and Protein Corona Formation. *Small* **2020**, *16*, 2002162, doi:10.1002/smll.202002162.
20. Nienhaus, K.; Nienhaus, G.U. Mechanistic Understanding of Protein Corona Formation around Nanoparticles: Old Puzzles and New Insights. *Small* **2023**, *19*, 2301663, doi:10.1002/smll.202301663.
21. Fam, S.Y.; Chee, C.F.; Yong, C.Y.; Ho, K.L.; Mariatulqabtiah, A.R.; Tan, W.S. Stealth Coating of Nanoparticles in Drug-Delivery Systems. *Nanomaterials* **2020**, *10*, doi:10.3390/nano10040787.
22. Chen, Q.; Wang, C.; Cheng, L.; He, W.; Cheng, Z.; Liu, Z. Protein Modified Upconversion Nanoparticles for Imaging-Guided Combined Photothermal and Photodynamic Therapy. *Biomaterials* **2014**, *35*, 2915–2923, doi:10.1016/j.biomaterials.2013.12.046.
23. Shanwar, S.; Liang, L.; Nechaev, A.V.; Bausheva, D.K.; Balalaeva, I.V.; Vodeneev, V.A.; Roy, I.; Zvyagin, A.V.; Guryev, E.L. Controlled Formation of a Protein Corona Composed of Denatured BSA on Upconversion Nanoparticles Improves Their Colloidal Stability. *Materials (Basel)* **2021**, *14*, 1657, doi:10.3390/ma14071657.
24. Ezerskyte, E.; Morkvenas, A.; Venius, J.; Sakirzanovas, S.; Karabanovas, V.; Katelnikovas, A.; Klimkevicius, V. Biocompatible Upconverting Nanoprobes for Dual-Modal Imaging and Temperature Sensing. *ACS Appl. Nano Mater.* **2024**, *7*, 6185–6195, doi:10.1021/acsanm.3c06111.
25. Zheng, J.; Zhang, C.; Dickson, R.M. Highly Fluorescent, Water-Soluble, Size-Tunable Gold Quantum Dots. *Phys Rev Lett* **2004**, *93*, 077402, doi:10.1103/PhysRevLett.93.077402.
26. Kun, R.; Szekeres, M.; Dekany, I. Isothermal Titration Calorimetric Studies of the pH Induced Conformational Changes of Bovine Serum Albumin. *Journal of Thermal Analysis and Calorimetry* **2009**, *96*, 1009–1017, doi:10.1007/s10973-009-0040-5.
27. Vicente-Escobar, J.O.; García-Sánchez, M.A.; González, F.; Cipagauta-Díaz, S.; Estrella González, A. A Spectroscopic and Molecular Docking Study of Interactions of Tetracarboxyphenyl Porphyrin and Chlorin E6 with Bovine Serum Albumin. *Chem. Pap.* **2021**, *75*, 4501–4515, doi:10.1007/s11696-021-01670-3.
28. Dukhno, O.; Przybilla, F.; Collot, M.; Klymchenko, A.; Pivovarenko, V.; Buchner, M.; Muhr, V.; Hirsch, T.; Mély, Y. Quantitative Assessment of Energy Transfer in Upconverting Nanoparticles Grafted with Organic Dyes. *Nanoscale* **2017**, *9*, 11994–12004, doi:10.1039/c6nr09706e.
29. Qiu, H.; Tan, M.; Ohulchanskyy, T.Y.; Lovell, J.F.; Chen, G. Recent Progress in Upconversion Photodynamic Therapy. *Nanomaterials* **2018**, *8*, doi:10.3390/nano8050344.

 doi:10.20944/preprints202603.1240.v1

30. Wang, Y.-F.; Liu, G.-Y.; Sun, L.-D.; Xiao, J.-W.; Zhou, J.-C.; Yan, C.-H. Nd3+-Sensitized Upconversion Nanophosphors: Efficient In Vivo Bioimaging Probes with Minimized Heating Effect. *ACS Nano* **2013**, *7*, 7200–7206, doi:10.1021/nn402601d.
31. Chan, M.-H.; Pan, Y.-T.; Lee, I.-J.; Chen, C.-W.; Chan, Y.-C.; Hsiao, M.; Wang, F.; Sun, L.; Chen, X.; Liu, R.-S. Minimizing the Heat Effect of Photodynamic Therapy Based on Inorganic Nanocomposites Mediated by 808 Nm Near-Infrared Light. *Small* **2017**, *13*, 1700038, doi:10.1002/smll.201700038.
32. Abrahamse, H.; Hamblin, M.R. New Photosensitizers for Photodynamic Therapy. *Biochem J* **2016**, *473*, 347–364, doi:10.1042/BJ20150942.
33. Kari, S.; Subramanian, K.; Altomonte, I.A.; Murugesan, A.; Yli-Harja, O.; Kandhavelu, M. Programmed Cell Death Detection Methods: A Systematic Review and a Categorical Comparison. *Apoptosis* **2022**, *27*, 482–508, doi:10.1007/s10495-022-01735-y.